Statistical analyzing the effect of ionospheric irregularity on GNSS radio occultation atmospheric measurement

Mingzhe Li [1,2,3,4], Xinan Yue [1,2,3,4]

[1] Key Laboratory of Earth and Planetary Physics, Institute of Geology and Geophysics, Chinese Academy of Sciences, Beijing, China

[2] Innovation Academy for Earth Science, CAS, Beijing, China

[3] Beijing National Observatory of Space Environment, Institute of Geology and Geophysics, Chinese Academy of Sciences, Beijing, China

[4] College of Earth and Planetary Sciences, University of Chinese Academy of Sciences, Beijing, China

Correspondence to: Xinan Yue (yuexinan@mail.iggcas.ac.cn)

Abstract. The Global Navigation Satellite System (GNSS) atmospheric radio occultation (RO) has been an effective method for Earth's atmosphere exploring. RO signals propagate through ionosphere before reaching the neutral atmosphere. The GNSS signal is affected by the ionospheric irregularity including the sporadic E (Es) and the F region irregularity due to mainly multipath effect. The effect of ionospheric irregularity on atmospheric RO data has been demonstrated by several studies in terms of cases. However, its statistical effect has not been investigated comprehensively. In this study, based on the Constellation Observing System for Meteorology, Ionosphere, and Climate (COSMIC) RO data during 2011-2013, the failed inverted RO events occurrence rate and the bending angle oscillation, which is defined as the standard deviation of the bias between the observed bending angle and the National Center for Atmospheric Research (NCAR) climatology model bending angle between 60 and 80 km, were used for statistical analysis. It is found that in middle and low latitudes during the daytime, the failed inverted RO occurrence and the bending angle oscillation show obvious latitude, longitude, and local time variations, which correspond well with the Es occurrence features. The F region irregularity (FI) contributes to the obvious increase of the failed inverted RO occurrence rate and the bending angle oscillation value during the nighttime over the geomagnetic equatorial regions. For high latitude regions, the Es can increase the failed inverted RO occurrence rate and the bending angle oscillation value during the nighttime. There also exists the seasonal dependency of the failed inverted RO event and the bending angle oscillation. Overall, the ionospheric irregularity effects on GNSS atmospheric RO measurement

30 exist in terms of failed RO event inversion and bending angle oscillation statistically. Awareness of these

31 effects could benefit both the data retrieval and applications of RO in the lower atmosphere.

32

33 **1. Introduction**

34 The radio occultation (RO) is a technique originally developed in the late 1960s and early 1970s for

35 planetary atmosphere exploring. With the great development of the Global Navigation Satellite System

36 (GNSS) over the past 30 years, the GNSS signal has been an effective source for exploring the Earth's

37 atmosphere. Several RO missions such as the Global Positioning System Meteorology (GPS/MET), the

38 Challenging Minisatellite Payload (CHAMP) (Wickert et al., 2001), the Scientific Application Satellite-

39 C (SAC-C), the Gravity Recovery and Climate Experiment (GRACE) (Beyerle et al., 2005), the

40 Constellation Observing System for Meteorology, Ionosphere and Climate (COSMIC) (Schreiner et al.,

41 2007), the Meteorological Operational Satellite Program (Metop) A/B, the Fengyun-3C (FY-3C) (Mao

42 et al., 2016) and et al have proven the good capability of RO for observing the Earth's ionosphere and

43 atmosphere. High-quality products of RO have been used for space weather, weather and climate

44 research (Anthes et al., 2008).

45

46 The RO technique could be divided into the ionospheric RO and the atmospheric RO. For the former one,

47 the GNSS signal propagates through the ionosphere. Dual-frequency pseudo-range and carrier phase can

48 be observed by the receiver onboard the low Earth orbit (LEO) satellite and be used to invert the electron

49 density profile. Besides, the amplitude and phase measurements can be used to calculate the ionospheric

50 scintillation index such as the S4 index. The S4 index is defined as the standard deviation of the received

51 signal power normalized to the average signal power, it can represent the occurrence of the ionospheric

52 irregularity (Yue et al., 2016). For the latter one, the GNSS signal propagates through both the ionosphere

53 and the neutral atmosphere. The dual-frequency carrier phase can be used to calculate the bending angle

54 and then invert the atmospheric parameters. As a result, the effects on signals caused by the ionosphere

55 should be removed before deriving the atmospheric RO products.

56

57 For atmospheric RO, the GNSS signal is mainly affected by the ionosphere in two ways. Firstly, the

58 existence of dense ionospheric electron density contributes to the bending of signals. Similar to the first-

59 order ionospheric term calibration used in ground-based dual-frequency observations, a linear

60 combination of the two-band signal bending at the same impact parameter is usually used to remove the

61 ionospheric effect (Vorob'ev and Krasil'nikova, 1994). However, after the linear combination of bending

62 angles, there still exists a residual ionospheric error (RIE). The RIE could bring ionospheric variability

63 such as solar cycle, local time, and seasonal variations into atmospheric RO products although its

64 amplitude is relatively low (Li et al., 2020). It means that the climate research using atmospheric RO

65 products would be affected by the ionosphere. Some efforts have been tried for the RIE calibration

66 (Danzer et al., 2013, 2015, 2020; Healy and Culverwell, 2015; Angling et al. 2018; Liu et al., 2018, 2020;

67 Li et al., 2020). Danzer et al. (2013) have analyzed the bending angle bias of CHAMP and COSMIC RO

68 data from 2001-2011 and tried to parameterize bending angle bias versus the solar cycle to make

69 statistical corrections. Healy and Culverwell (2015) found a good correlation between the RIE and the

70 difference of GPS L1 and L2 bending angles at the same impact parameter. They then proposed a

71 correction method using the 'kappa' parameter under the ionospheric spherical symmetry assumption.

72 This method was further tested by Danzer et al. (2015), Angling et al. (2018) and Danzer et al. (2020). It

73 can reduce the systematic errors vary with solar cycle from 0.2 K to 2.0 K at altitudes between 40 km to

74 45 km. Liu et al. (2018) have analyzed the ionospheric structure influences on RIE in bending angles

75 based on ray tracing simulations and further developed a "Bi-local correction approach" to calculate the

76 RIE through an equation. This method considers both the ionospheric asymmetry effects as well as the

77 geomagnetic effects on bending angles (Liu et al., 2020). In our previous study, we have also

78 characterized the RIE effects statistically by both ray-tracing simulation and data analysis (Li et al., 2020).

79 Secondly, the small-scale irregularities in the ionosphere also have an impact on the GNSS signal and

80 finally affect the atmospheric RO products. The small-scale irregularities of which interest to this study

81 are the sporadic E (Es) and the F region irregularity (FI). As indicated by former studies, the ionospheric

82 irregularity will cause refraction or diffraction of the GNSS signal during its propagating through the

83 ionosphere. The received signals could show temporal fluctuations in both amplitude and phase, which

84 is known as the ionospheric scintillation. The impact of the small-scale irregularity on atmospheric RO

85 can be significant but show quite different climatological characteristics in comparison with the large-

86 scale ionospheric effects (Li et al., 2020). Besides, it is difficult to model the ionospheric irregularity in

87 a deterministic fashion for simulation research (Mannucci, et al., 2011). Previous studies only pointed

88   out this small scale ionospheric effect in terms of cases (Zeng and Sokolovskiy, 2010). To our knowledge,

89   there is no comprehensive study giving statistical analysis between ionospheric irregularity and

90   atmospheric RO products, which is quite important to quantify this effect and therefore benefit

91   atmospheric RO data retrieval and application. This is the main objective of this study.

92

93   In the following sections, we try to study the ionospheric irregularity effects on GNSS atmospheric RO

94   measurement statistically. Based on previous related studies, the current study will make sense as

95   following advantages: (1) the correlation between failed inverted COSMIC RO events and the

96   ionospheric irregularity are analyzed; (2) morphology of the bending angle oscillation in the atmospheric

97   RO measurement are presented in comparison with the occurrence rate of both Es and FI; (3) the seasonal

98   dependency of failed inverted RO events and the bending angle oscillation is analyzed. We will describe

99   the COSMIC observation and the statistical method in Section 2 and Section 3, respectively. Then the

100 ionospheric irregularity effects on single RO cases will be shown in Section 4. The statistical results of

101 the failed inverted RO event and the bending angle oscillation will be depicted in comparison with the

102 ionospheric irregularity occurrence rate in Section 5. Finally, the conclusions and implications will be

103 presented in Section 6.

104

105 **2. RO Data Description**

106 COSMIC, as one of the most successful RO missions, was launched on 15 April 2006. The constellation

107 with six LEO satellites has contributed millions of profiles for space weather, weather, and climate

108 research in the past 14 years. Each COSMIC satellite has four separate antennas: two high gain

109 occultation antennas received GNSS signals with a 50 Hz sampling rate to explore the neutral atmosphere

110 from the top (~130 km) to bottom or reverse. The carrier phase modulated on signals can be used for

111 excess phase calculating and atmospheric parameters retrieving. The other two antennas are precise orbit

112 determination (POD) antennas with a 1 Hz sampling rate. The received signals are used for LEO orbiting,

113 ionosphere electron density, slant total electron content (TEC), and scintillation index calculating

114 (Schreiner et al., 2007, 2011). The COSMIC data are processed by the COSMIC Data Analysis and

115 Archive Center (CDAAC) of the University Corporation for Atmospheric Research (UCAR) and

116 available on the CDAAC website (http://cdaac-www.cosmic.ucar.edu/). In this study, the COSMIC RO

117 observations during 2011-2013 were used for analysis. The S4 scintillation index in auxiliary data file

118 (scnLv1) was used for the Es and FI occurrence rates calculation. The dry atmospheric profiles file

119 (atmPrf) was used for the failed inverted RO occurrence rate calculation and the atmospheric bending

120 angle oscillation morphology analysis. The specific calculating method will be introduced in the

121 following section.

122

123 **3. Analysis Method**

124 To study the ionospheric irregularity effects on RO, we focus on analyzing two parameters: the failed

125 inverted RO event occurrence rate and the bending angle oscillation defined as the mean standard

126 deviation of the bias between the observed bending angle and the NCAR climatology model bending

127 angle during the 60-80 km altitude interval. The failed inverted RO event means those events flunked

128 the quality control during profiles inversion in CDAAC. They are identified by the 'bad' attribute in the

129 atmPrf file whose values are equal to 1. The oscillation of atmospheric RO bending angle is also provided

130 by the atmPrf file. The S4 index contained in the scnLv1 file is used to represent the occurrence of the

131 ionospheric irregularity. The occurrence rate of S4 index larger than 0.3 is set to represent the occurrence

132 of ionospheric irregularity. It should be noted that we identify the occurrence altitude range between

133 50~600 km as the contribution of both Es and FI together. We first calculated the failed inverted RO

134 event occurrence rate in comparison with the ionospheric irregularity occurrence rate. After that, failed

135 inverted RO events of COSMIC during 2011-2013 were screened out to study the Es and FI effects on

136 the bending angle observation. Additionally, the ionPrf file of CDAAC is used for displaying the electron

137 density profiles in single cases.

138

139 **4. Ionospheric Irregularity Effect on Single RO Cases**

140 To have a preliminary knowledge of the ionospheric irregularity effect on atmospheric RO, we firstly

141 show several typical single case examples. The results are shown in Figure 1. From top to bottom, each

142 row show results of a case. The three cases represent the RO event without ionospheric irregularity, the

143 RO event affected by the Es, and the event affected by the FI, respectively. From left to right columns,

144 the panels represent the inverted bending angles, the signal-to-noise ratio (SNR) of L1 C/A signal, the

145 related electron density profile, and the inverted dry temperature profile compared with the European

146 Centre for Medium-Range Weather Forecasts (ECMWF) results. Please note that the grey lines in the

147 rightmost panels denote the results of RO inverted temperature and the red lines represent those of

148 ECMWF. The purple lines in case 1 and case 3 are the temperature bias multiplied by 10 for convenient

149 comparison. The features of L1 C/A SNR profile and the electron density profile could identify whether

150 a RO event is affected by the ionospheric irregularity (Yue et al., 2015). As depicted in the second column,

151 the case 2 shows visible peaks in SNR fluctuation around 110 km, which correspond to the occurrence

152 altitude range of Es and could reflect the Es effects on this event. Besides, the electron density profile of

153 case 3 shows obvious scintillation between 200 km and 300 km, which implies the FI impact on signals.

154 We also use the corresponding CDAAC scnLv1 file for verification. The S4 maximum values of cases

155 1-3 are 0.03, 0.59, and 1.21, with S4 peaks around 111.69, 108.45, and 274.86 km, respectively. It can

156 be seen that the normal case shows good inversion results. The value of the ionospheric-corrected LC

157 bending angle above 40 km is much smaller than those of the L1 and L2 bending angles. It means that

158 the ionosphere dominates the bending of the RO signal in this tangent altitude interval and the linear

159 combination method works well. The bias between the observed dry temperature and the ECMWF result

160 is insignificant. However, the Es case shows bad results. Values of the inverted L2 bending angle are

161 negative, which leads to larger values of LC bending angle after the linear combination. As a result, the

162 temperature profile is failed inverted. Significant temperature bias between the observation and model

163 result can be seen from the rightmost panel. For the FI case, oscillations can be seen in the LC bending

164 angle profile in the leftmost panel as well as the temperature bias profile in the rightmost panel. The

165 bending angle oscillation values of cases 1-3 are 0.66, 16.06, and 5.74 μrad, respectively. It indicates

166 that this oscillation could also be related to the ionospheric irregularity. The geometry of atmospheric

167 RO observation determines that the ionospheric irregularity effects could propagate to a deep tangent

168 height, where far below the altitude range of irregularity occurrence (Wu, 2020). We have gone through

169 many cases and found that the failed inverted RO event and strong bending angle oscillation occurs

170 usually along with Es and FI occurrence. But not all events affected by the Es and FI are failed inverted.

171 The analysis of single cases motivates our further statistical study.

172

173 **5. Statistical Results**

174 The Es and FI have been investigated comprehensively in the past several decades (Hocke et al., 2001;

175   Straus et al., 2003; Wu, 2005; Arras et al., 2008, 2009; Carter et al., 2013; Yue et al., 2015, 2016).

176   Generally, the Es can be seen as thin layers with much higher plasma density than the normal E region

177   density occurring during the altitude range of ~ 90-120 km. The occurrence rate of Es is controlled by

178   many factors such as the tidal wind, the Earth's geomagnetic field, and metal ions (Axford, 1963; Chu et

179   al., 2014). These factors lead to the complicated variations of Es along with latitude, longitude, altitude,

180   local time, and season (Hocke et al., 2001; Wu, 2005; Arras et al., 2008, 2009). FI is the plasma

181   irregularity and inhomogeneity in the F region caused by plasma instabilities (Dungey, 1956; Fejer and

182   Kelley, 1980). The scale sizes of the density irregularity range from a few centimeters to hundreds of

183   kilometers and the irregularity can appear at all latitudes. Both Es and FI have been observed by

184   ionosonde, incoherent/coherent scatter radars, and ground-based GNSS networks. Since the success of

185   GPS/MET, the GNSS RO has also been proven as an effective technique to detect the occurrence of Es

186   and FI. Hocke et al. (2001) first derived the occurrence of Es from the GPS/MET observation and

187   confirmed its seasonal variation. Wu (2005) studied the latitude, local time, altitude, and seasonal

188   dependency of Es by using CHAMP occultation data. Arras et al. (2008) further investigated the

189   occurrence of Es using multiple RO missions including CHAMP, GRACE-A, and COSMIC. Chu et al.

190   (2014) presented the morphology of Es based on COSMIC amplitude and phase fluctuations of L-band

191   signals. For FI, Straus et al. (2003) made a statistical analysis of the GPS C/A code SNR fluctuations on

192   L1 frequency based on observations onboard the PICOSat satellite. They found that the geographic and

193   local time distributions of occultation having large values of the S4 index were consistent with known

194   scintillation climatology. Brahmanandam et al. (2012) presented the three-dimensional global

195   morphology and seasonal variations of S4 index measured from COSMIC for a low solar activity year

196   2008 and found the latitude, altitude, and local time dependency of FI. Carter et al. (2013) further

197   revealed the longitudinal and seasonal variations of equatorial FI using COSMIC S4 index. Besides, Yue

198   et al. (2015, 2016) also studied the complex Es and the ionospheric irregularity related GPS RO loss of

199   lock by COSMIC S4 index.

200

201   As investigated in the single case section, the failed inverted RO event and bending angle oscillation

202   could be related to the ionospheric irregularity. So we carried out statistical research from all COSMIC

203   atmospheric events during 2011-2013. Firstly, the RO event whose 'bad' attribute in the atmPrf file equals

204   to 1 was selected as the failed inverted RO for the statistics. Then the failed inverted RO events were

205   screened out for the bending angle oscillation study. The geographical and geomagnetic distributions of

206   Es and FI are plotted separately in Figure 2. The mixed Es and FI occurrence rate, the failed inverted RO

207   event occurrence rate and the bending angle oscillation are shown in Figure 3. The grid resolutions are

208   10° ×3° for Lon×Lat and 3° ×2 h for MLat×MLT, respectively.

209

210   As depicted in Figure 3, the global geographical distribution of both Es and FI occurrence rate together

211   is depicted in the top left panel. For low and middle latitudes, two peaks of Es occurrence rate locate in

212   the East Asia region and the North Africa region in the northern hemisphere. One peak locates near the

213   South America region. The values of occurrence rate are greater than 30% in peak regions. One trough

214   can be seen around the South Africa region with an occurrence rate lower than 10%. The result

215   corresponds well with the Es characteristics derived from the GPS RO phase and SNR fluctuations (Wu,

216   2005). Besides, an occurrence enhancement can be seen around the West Africa and the Atlantic Ocean

217   region, which agrees with the previous studies base on COSMIC S4 index (Brahmanandam et al., 2012;

218   Yue et al., 2016) and indicates the contributions of FI. For high latitudes, two peaks are available during

219   120° W-150° W and 0°-60° E in the northern hemisphere and one peak can be seen around 120° E near

220   North Antarctica. In the top middle panel, we plotted the occurrence rate of failed inverted RO events

221   during 2011-2013. The rate represents the failed inverted RO event in percentage which was calculated

222   based on all observed COSMIC RO events during this time interval. Overall, the global distribution of

223   the failed inverted RO event occurrence agrees with those of the Es occurrence in the top left panel. Two

224   peaks in the northern hemisphere and one in the southern hemisphere match the locations of Es

225   occurrence peaks around ±20°. Besides, there exists an obvious increase in the failed inverted RO events

226   in high latitudes. It should be noted that the occurrence rate distribution of failed inverted RO events

227   can't match those of Es and FI completely because the inversion error is not only affected by the

228   ionospheric irregularity but also affected by other factors such as the low SNR. However, the contribution

229   of FI on the failed inverted RO event is not obvious in this panel. This might be due to the high occurrence

230   regions of FI overlaps those of Es partly. In the top right panel, we plotted the global distributions of the

231   median bending angle oscillation. The results are also in good agreement with those patterns of Es and

232   FI occurrence rate. Strong oscillations can be seen around North Africa and the East Asia regions in the

233   Northern Hemisphere and around South America in the Southern Hemisphere, with bending angle

234   oscillation values of ~1.4 μrad. The trough of bending angle oscillation can be seen around the South

235   Africa regions with values less than 1 μrad. Both the locations of peaks and troughs correspond well

236   with those of Es occurrence rate. Besides, larger oscillation values are available in the Atlantic Ocean

237   around the equator, which could be related to the high FI occurrence in these regions. Especially, both

238   the failed inverted RO and the bending angle oscillation show obvious peaks around 120° E near North

239   Antarctica. Peaks of the two parameters could be related to the high occurrence of both Es and FI in this

240   region. Peaks of Es and FI occurrence in this region have also been observed by Wu (2020) based on S4

241   index from RO data sets.

242

243   We also plotted the geomagnetic local time and latitude (MLT-MLat) distribution of the three parameters

244   in the bottom panels in Figure 3 for further comparison. In most regions of the bottom left panel, the

245   distributions are similar to those of the Es. Irregularity occurs more around geomagnetic equator regions

246   and the aurora oval regions. Around the geomagnetic equator regions during 18-24 MLT, there is an

247   occurrence enhancement caused by FI. Both Es and FI contribute to a 'three peaks' feature in the equator

248   regions after sunset. These features correspond to the previous studies observed no matter by ground-

249   based GNSS observations (Li et al., 2011) or COSMIC RO observations (Chen and Huang, 2017).

250   Similar features can be seen in the bottom middle panel. The occurrence rate of the failed inverted RO

251   event is higher around the equator regions from sunset to midnight, which can reach 20%. In high

252   latitudes, two ovals are available. Besides, the failed inverted RO event also occurs more after midnight

253   and during the noon in the Southern Hemisphere. In these regions, the FI could make contributions. For

254   bending angle oscillation in the bottom right panel, three peaks of the mean oscillation value exist along

255   the geomagnetic latitude, which denotes the contribution of Es and FI during the nighttime. The value of

256   bending angle oscillation tends to be small within $\pm 60°$ during 2~10 MLT. For high latitudes, the

257   bending angle shows strong oscillation even though the occurrence rate of Es and FI is lower than those

258   of peak regions in middle and low latitudes.

259

260   For a better display of the high-latitude results, we plotted the irregularity and failed inverted RO

261   occurrence rates as well as the bending angle oscillation variation with MLT-MLat in northern and

262   southern polar regions in Figure 4. As depicted in the left two panels, the ionospheric irregularity mainly

263   occurs during 18-24 MLT, with occurrence peaks existing in aurora regions around midnight and moving

264   toward the polar cap regions when approaching the sunset time. Values of the irregularity occurrence rate

265   are around 10-20% during the nighttime and can reach 30% for peak regions. The middle two panels

266   show the occurrence rate of failed inverted RO events. It is depicted that the peaks are located in aurora

267   regions and extent to the polar cap regions from sunset time to midnight. The increase in the occurrence

268   rate around these regions might be affected by the high occurrence rate of Es. The failed inverted RO

269   occurrence rates are also higher during the daytime in both hemispheres although the irregularity

270   occurrence rates are lower than 10% during this period. The right panels show the bending angle

271   oscillation results. Its value is larger in aurora regions around midnight, which can reach 2.1 µrad. For

272   those values in the South Hemisphere, strong bending angle oscillation can be seen in the polar cap

273   regions no matter during the daytime or nighttime. Besides, the peak regions locate mainly between

274   80° S-90° S instead of the 70° S-80° S as the irregularity occurrence peak shown in the bottom middle

275   panel.

276

277   We also use the scatter plot to study correlations between the ionospheric irregularity and the two

278   parameters. The results were plotted in Figure 5. Considering patterns of the failed inverted RO

279   occurrence rate and the bending angle oscillation could not agree very well with those of the irregularity

280   in high latitude regions, we mainly pay attention to the results in low and middle latitudes (60° S-60° N).

281   Correlations during the daytime (6~18 MLT) and the nighttime (0~6, 18~24 MLT) were displayed

282   respectively. Overall, the correlations between the ionospheric irregularity and the two parameters are

283   significant although they are not strictly linear especially for the bending angle oscillation during the

284   daytime. The scatters in the panels are probably due to that the failed inverted RO and the bending angle

285   oscillation are not only affected by the Es and FI but also related to other factors. For example, the sudden

286   stratospheric warming events can make the atmospheric structure changes significantly and far from the

287   climatology. As a result, bias between the RO observation and the climatological model could be

288   increased and lead to the atmosphere RO event is identified as "Bad" during inversion. Considering the

289   sudden stratospheric warming events often occur over the polar winter (Butler et al., 2015), they could

290   also contribute to the pattern difference between the ionospheric irregularity occurrence rate and the two

291   parameters in Figure 4. Meanwhile, the observation and inversion noise could also make contributions.

292

293   In Figures 3-5, we mainly concern about the yearly average pattern. As stated above, the seasonal

294   variation of irregularity has been confirmed by previous studies (Arras et al., 2008; Chen and Huang,

295   2017). So the seasonal dependency of the failed inverted RO event and the bending angle oscillation

296   could also exist. For further investigating, the occurrence rate variation with Lon-Lat and MLT-MLat

297   were depicted in Figure 6 and Figure 7, respectively. Equinox (March, April, September, and October),

298   Northern Summer (May, June, July, and August), and Northern Winter (January, February, November,

299   and December) are considered here. Generally, in Figure 6, the distributions of the failed inverted RO

300   event occurrence are in good agreement with those of the irregularity. Both parameters are larger within

301   ±30° in Equinox and larger in summer than in winter. For Northern Summer, the occurrence peaks are

302   near the North Africa area and the East Asia area. For Northern Winter, the peaks are available in the

303   Pacific Ocean regions nearby South America. Similar to the average pattern in Figure 3, the failed

304   inverted RO occurrence rate is high in polar regions even though the Es and FI occurrence is not obvious

305   in comparison with those of peak regions in low latitudes. The MLT-MLat distributions of the irregularity

306   and the failed inverted RO in Figure 7 also show similar seasonal variations. But for the southern polar

307   region in Equinox and the northern polar region in Northern Winter, the failed inverted RO occurs

308   significantly on condition that the occurrences of Es and FI are not obvious. For the bending angle results

309   in both bottom panels in Figures 6 and 7, it is apparent that the bending angle oscillation value also

310   follows a similar seasonal variation with the ionospheric irregularity occurrence, which is larger in

311   summer than in winter with the equinox as the transitory season. It is noticeable that for the geographic

312   distribution, larger values exist around Northern Antarctica in all seasons. For the geomagnetic

313   distributions, the three peaks along geomagnetic latitudes are available in all seasons.

314

315   **6.   Conclusions and Implications**

316   In this paper, we focus on the ionospheric irregularity effects on GNSS atmospheric RO. The failed

317   inverted RO events and the bending angle oscillation are the two main parameters we concern about. The

318   COSMIC S4 index provided by CDAAC during 2011-2013 is used to characterize the ionospheric

319   irregularity occurrence rate such as the Es and the F region irregularity. The 'bad' attribute in the atmPrf

320   file is used to identify the failed inverted RO events on condition that its value equals to 1. The mean

321   bending angle oscillation also from the atmPrf file is used to reflect the degree of bending angle

322   oscillation. Results from single cases are analyzed firstly. Then the distribution patterns and seasonal

323   variations of the ionospheric irregularity occurrence rate, failed inverted RO event occurrence rate, and

324   the bending angle oscillation are presented for the correlation study. The main conclusions and

325   implications of the paper are summarized in the following:

326   (1) The ionospheric irregularity such as the Es and the F region irregularity could affect the GNSS

327   atmospheric RO in terms of causing failed inverted RO events and the bending angle oscillation in

328   both cases and statistically.

329   (2) In middle and low latitudes, during the daytime, both the failed inverted RO event and the bending

330   angle oscillation are mainly affected by the Es. During the nighttime, the F region irregularity

331   contributes to the obvious increases of the failed inverted RO occurrence rate and the bending angle

332   oscillation around the geomagnetic equatorial regions.

333   (3) In the polar regions, the Es mainly affect the two parameters in the aurora regions from sunset to

334   midnight. But the correlations between the ionospheric irregularity and the two parameters are not

335   as obvious as those in middle and low latitudes.

336   (4) Seasonal dependency of the failed inverted RO occurrence and the bending angle oscillation exists,

337   which also accord well with the seasonal variation of the Es and the F region irregularity.

338   (5) The occurrence rate of the failed inverted RO can reach 15% in low latitudes and even 20% in peak

339   regions. It means that hundreds of COSMIC RO events per day will be ruled out during quality

340   control. The bending angle oscillation between 60 and 80 km also varies from ~0.6 μrad in trough

341   regions to ~2.5 μrad in peak regions. Although 60~80 km is not the main altitude range of RO data,

342   the small-scale effects in atmospheric RO exist in all altitudes and could affect the atmospheric

343   research related to RO products. Awareness of the ionospheric irregularity effect on RO could be

344   beneficial to improve the data retrieval, quality control of GNSS atmospheric RO data processing

345   and data assimilation application in numerical weather prediction (Cardinali and Healy, 2014).

346

347   Overall, the ionospheric irregularity effects on GNSS atmospheric RO measurement exist. The effects

348 can lead to the failed inverted RO event and the bending angle oscillation. A suitable filter may be

349 effective in calibrating these effects and improving the quality of atmospheric RO products. We hope to

350 investigate the potential calibrating method in our further work.

351

352 **7. Acknowledgement**

353 This work was supported by the B-type Strategic Priority Program of the Chinese Academy of Sciences

354 (Grant No. XDB41000000), the Open Research Project of Large Research Infrastructures - "Study on

355 the interaction between low/mid-latitude atmosphere and ionosphere based on the Chinese Meridian

356 Project", the National Natural Science Foundation of China (41427901), and the Key Research Program

357 of the IGGCAS with Grant No. IGGCAS-201904. The University Corporation for Atmospheric Research

358 (UCAR) COSMIC Data Analysis and Archive Center (CDAAC) is appreciated for processing and

359 sharing the COSMIC radio occultation data to the community over years. All the data used in the study

360 could be downloaded from the CDAAC website (http://cdaac-www.cosmic.ucar.edu/).

361

362 **8. References**

363 Axford, W. I.: The formation and vertical movement of dense ionized layers in the ionosphere due to

364 neutral wind shears, Journal of Geophysical Research, 68, 769–779, doi:10.1029/JZ068i003p00769,

365 1963.

366 Anthes, R. A., Bernhardt, P. A., Chen, Y., Cucurull, L., Dymond, K. F., Ector, D., Healy, S. B., Ho, S. P.,

367 Hunt, D. C., Kuo, Y. H., Liu, H., Manning, K., McCormick, C., Meehan, T. K., Randel, W. J., Rocken,

368 C., Schreiner, W. S., Sokolovskiy, S. V., Syndergaard, S., Thompson, D. C., Trenberth, K. E., Wee, T. K.,

369 Yen, N. L., and Zeng, Z.: The COSMIC/FORMOSAT-3 mission: Early results, Bulletin of the American

370 Meteorological Society, 89, 313–333, doi.org/10.1175/BAMS-89-3-313, 2008.

371 Angling, M. J., Elvidge, S., and Healy, S. B.: Improved model for correcting the ionospheric impact on

372 bending angle in radio occultation measurements, Atmospheric Measurement Techniques, 11, 2213-2224,

373 doi.org/10.5194/amt-11-2213-2018, 2018.

374 Arras, C., Wickert, J., Beyerle, G., Heise, S., Schmidt, T., and Jacobi, C.: A global climatology of

375 ionospheric irregularities derived from GPS radio occultation, Geophysical Research Letters, 35,

376   doi:10.1029/2008gl034158, 2008.

377   Arras, C., Jacobi, C., and Wickert, J.: Semidiurnal tidal signature in sporadic E occurrence rates derived

378   from GPS radio occultation measurements at higher midlatitudes, Ann Geophys, 27, 2555–2563, 2009.

379   Beyerle, G., Schmidt, T., Michalak, G., Heise, S., Wickert, J., and Reigber, C.: GPS radio occultation

380   with GRACE: Atmospheric profiling utilizing the zero difference technique, Geophysical Research

381   Letters, doi.org/10.1029/2005gl023109, 2005.

382   Brahmanandam, P. S., Uma, G., Liu, J. Y., Chu, Y. H., Latha Devi, N.S.M.P., and Kakinami, Y.: Global

383   S4 index variations observed using FORMOSAT-3/COSMIC GPS RO technique during a solar minimum

384   year, Journal of Geophysical Research: Space Physics, 117, doi:10.1029/2012ja017966, 2012.

385   Butler, A.H., Seidel, D.J., Hardiman, S.C., Butchart, N., Birner, T., and Match, A.: Defining sudden

386   stratospheric warmings, Bulletin of the American Meteorological Society, 96, 1913–1928,

387   doi:10.1175/BAMS-D-13-00173.1, 2015.

388   Cardinali, C. and Healy, S.: Impact of GPS radio occultation measurements in the ECMWF system using

389   adjoint-based diagnostics, Quarterly Journal of the Royal Meteorological Society, 140, 2315-2320,

390   doi:10.1002/qj.2300, 2014.

391   Carter, B.A., Zhang, K., Norman, R., Kumar, V. V., and Kumar, S.: On the occurrence of equatorial F-

392   region irregularities during solar minimum using radio occultation measurements, Journal of

393   Geophysical Research: Space Physics, 118, 892-904, doi:10.1002/jgra.50089, 2013.

394   Chu, Y. H., Wang, C. Y., Wu, K. H., Chen, K. T., Tzeng, K. J., Su, C. L., Feng, W., and Plane, J. M. C.:

395   Morphology of sporadic E layer retrieved from COSMIC GPS radio occultation measurements: Wind

396   shear theory examination, Journal of Geophysical Research: Space Physics, 119, 2117-2136,

397   doi:10.1002/2013ja019437, 2014.

398   Chen, S. and Huang, Z.: Ionospheric F-layer global scintillation index variation using COSMIC during

399   the period of 2007–2013, GPS Solutions, 21, 1049-1058, doi:10.1007/s10291-016-0593-2, 2017.

400   Dungey, J. W.: Convective diffusion in the equatorial F region, Journal of Atmospheric and Terrestrial

401   Physics, 9, 304-310, doi.org/10.1016/0021-9169(56)90148-9, 1956.

402   Danzer, J., Scherllin-Pirscher, B., and Foelsche, U.: Systematic residual ionospheric errors in radio

403   occultation data and a potential way to minimize them, Atmospheric Measurement Techniques, 6, 2169-

404   2179, doi.org/10.5194/amt-6-2169-2013, 2013.

405   Danzer, J., Healy, S. B., and Culverwell, I. D.: A simulation study with a new residual ionospheric error

406   model, for GPS radio occultation climatologies, Atmospheric Measurement Techniques, 8, 3395-3404,

407   doi.org/10.5194/amt-8-3395-2015, 2015.

408   Danzer, J., Schwaerz, M., Kirchengast, G., and Healy, S. B.: Sensitivity analysis and impact of the kappa-

409   correction of residual ionospheric biases on radio occultation climatologies, Earth and Space Science, 7,

410   e2019EA000942, doi.org/10.1029/2019EA000942, 2020.

411   Fejer, B. G. and Kelley, M. C.: Ionospheric irregularities. Reviews of Geophysics, 18, 401–454,

412   doi:10.1029/RG018i002p00401, 1980.

413   Hocke, K., Igarashi, K., Nakamura, M., Wilkinson, P., Wu, J., Pavelyev, A., and Wickert, J.: Global

414   sounding of sporadic E layers by the GPS/MET radio occultation experiment, Journal of Atmospheric

415   and Solar-Terrestrial Physics, 63, 1973–1980, 2001.

416   Healy, S. B., Culverwell, I. D.: A modification to the standard ionospheric correction method used in

417   GPS radio occultation, Atmospheric Measurement Techniques, 8, 3385-3393, doi.org/10.5194/amt-8-

418   3385-2015, 2015.

419   Li, G., Ning, B., Abdu, M. A., Yue, X., Liu, L., Wan, W., and Hu, L.: On the occurrence of postmidnight

420   equatorial Fregion irregularities during the June solstice, Journal of Geophysical Research: Space

421   Physics, 116, doi:10.1029/2010ja016056, 2011.

422   Liu, C., Kirchengast, G., Sun, Y., Zhang, K., Norman, R., Schwaerz, M., Bai, W., Du, Q., and Li, Y.:

423   Analysis of ionospheric structure influences on residual ionospheric errors in GNSS radio occultation

424   bending angles based on ray tracing simulations, Atmospheric Measurement Techniques, 11, 2427-2440,

425   doi.org/10.5194/amt-11-2427-2018, 2018.

426   Liu, C., Kirchengast, G., Syndergaard, S., Schwaerz, M., Danzer, J., and Sun, Y.: New Higher-Order

427   Correction of GNSS RO Bending Angles Accounting for Ionospheric Asymmetry: Evaluation of

428   Performance and Added Value, Remote Sensing, 12, doi.org/10.3390/rs12213637, 2020.

429   Li, M., Yue, X., Wan, W., and Schreiner, W. S.: Characterizing Ionospheric Effect on GNSS Radio

Occultation Atmospheric Bending Angle, Journal of Geophysical Research: Space Physics, 125, doi.org/10.1029/2019JA027471, 2020.

Mannucci, A. J., Ao, C. O., Pi, X., and Iijima, B. A.: The impact of large scale ionospheric structure on radio occultation retrievals, Atmospheric Measurement Techniques, 4, 2837-2850, doi.org/10.5194/amt-4-2837-2011, 2011.

Mao, T., Sun, L., Yang, G., Yue, X., Yu, T., Huang, C., Zeng, Z., Wang, Y., and Wang, J.: First Ionospheric Radio-Occultation Measurements From GNSS Occultation Sounder on the Chinese Feng-Yun 3C Satellite, IEEE Transactions on Geoscience and Remote Sensing, 54, doi.org/1-10. 10.1109/TGRS.2016.2546978, 2016.

Straus, P. R., Anderson, P. C., and Danaher, J. E.: GPS occultation sensor observations of ionospheric scintillation, Geophysical Research Letters, 30, doi:10.1029/2002gl016503, 2003.

Schreiner, W., Rocken, C., Sokolovskiy, S., Syndergaard, S., and Hunt, D.: Estimates of the precision of GPS radio occultations from the COSMIC/FORMOSAT-3 mission, Geophysical Research Letters, 34, doi:10.1029/2006gl027557, 2007.

Schreiner, W., Sokolovskiy, S., Hunt, D., Rocken, C., and Kuo, Y. H.: Analysis of GPS radio occultation data from the FORMOSAT-3/COSMIC and Metop/GRAS missions at CDAAC, Atmospheric Measurement Techniques, 4, 2255-2272, doi:10.5194/amt-4-2255-2011, 2011.

Vorob'ev, V. V. and Krasil'nikova, T. G.: Estimation of the accuracy of the atmospheric refractive index recovery from Doppler shift measurements at frequencies used in the NAVSTAR system, USSR, Atmospheric and Oceanic Physics, English Translation, 29, 602-609, 1994.

Wickert, J., Marquardt, C., Beyerle, G., Reigber, C., and König, R.: Atmosphere sounding by GPS radio occultation: First results from CHAMP, Geophysical Research Letters, 28, 3263-3266. doi.org/10.1029/2001gl013117, 2001.

Wu, D. L.: Sporadic E morphology from GPS-CHAMP radio occultation, Journal of Geophysical Research, doi:10.1029/2004ja010701, 2005.

Wu, D. L.: Ionospheric S4 Scintillations from GNSS Radio Occultation (RO) at Slant Path, Remote Sensing, 12, doi:10.3390/rs12152373, 2020.

457 Yue, X., Schreiner, W. S., Zeng, Z., Kuo, Y. H., and Xue, X.: Case study on complex sporadic E layers

458 observed by GPS radio occultations, Atmospheric Measurement Techniques, 8, 225-236,

459 doi:10.5194/amt-8-225-2015, 2015.

460 Yue, X., Schreiner, W. S., Pedatella, N. M., and Kuo, Y. H.: Characterizing GPS radio occultation loss of

461 lock due to ionospheric weather, Space Weather, 14, 285-299, doi:10.1002/2015sw001340, 2016.

462 Zeng, Z. and Sokolovskiy, S.: Effect of sporadic E clouds on GPS radio occultation signals, Geophysical

463 Research Letters, 37, doi:10.1029/2010gl044561, 2010.

464
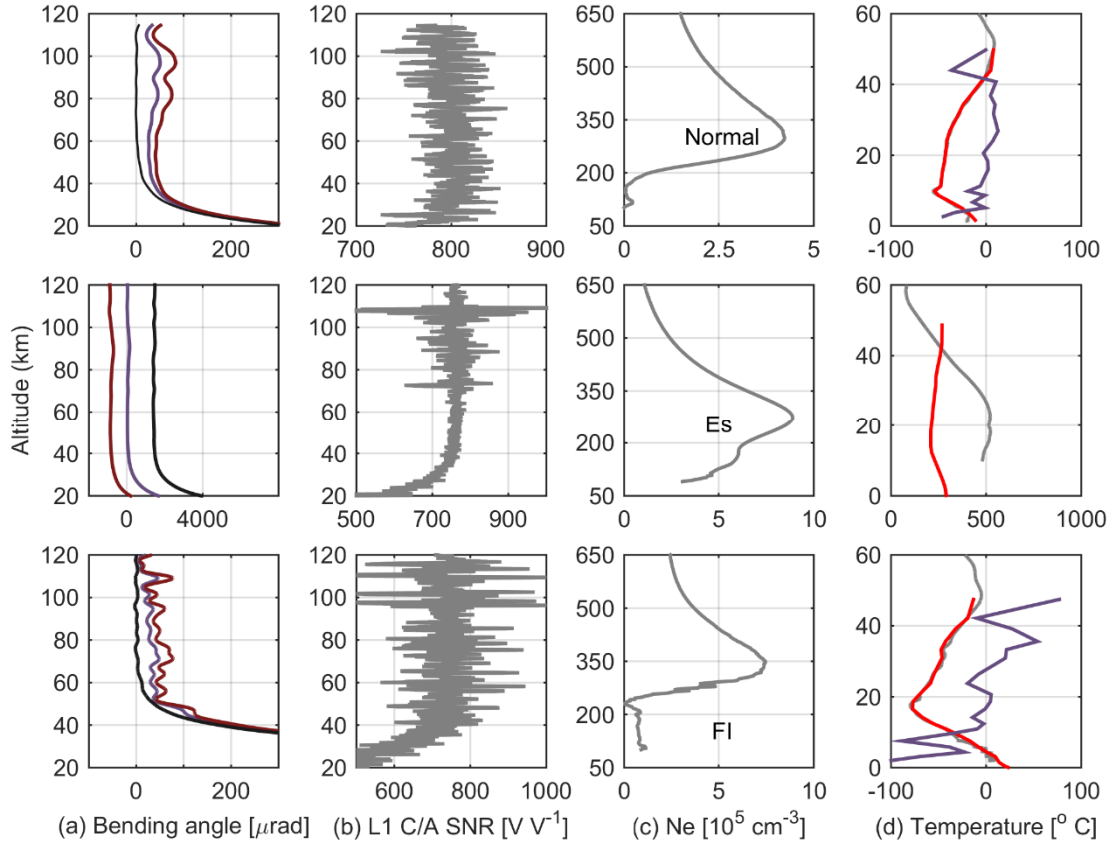
Figure 1. Example of three cases occurred in 2013 made by COSMIC. Panels from top to bottom are normal example without the ionospheric irregularity occurrence, the Es example, and the F region irregularity example. Panels from left to right are the inverted L1 (purple line), L2 (brown line), and LC (black line) bending angles; the L1 C/A SNR, the electron density profile at the RO tangent points; the inverted dry temperature (grey line) versus the ECMWF results (red line) as well as their bias multiplied by 10 (purple line). Please note that the Y-axis of all panels represents the altitude with kilometer (km) as the unit.
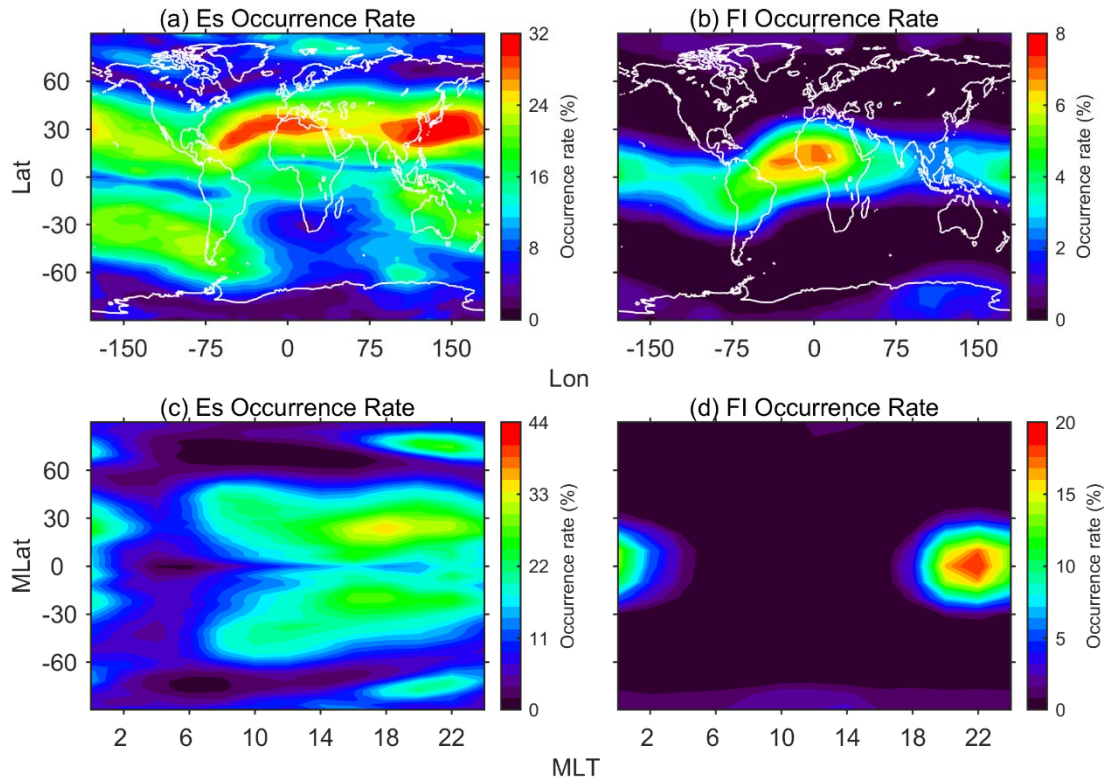
472
473 **Figure 2. Global geographical (top panels) and geomagnetic distributions (bottom panels) of the**
474 **Es (left panels) and F layer irregularity occurrence rate (right panels), during 2011-2013.**

475
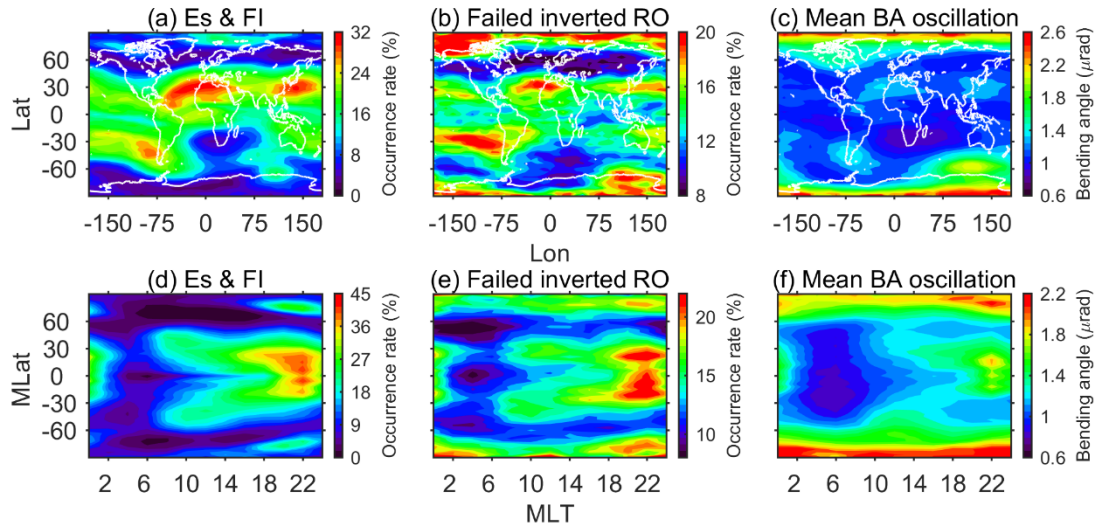
Figure 3. Global geographical (top panels) and geomagnetic distributions (bottom panels) of the Es and F layer irregularity occurrence rate (left panels), the failed inverted RO event occurrence rate (middle panels), and the mean bending angle oscillation (right panels) during 2011-2013.

480
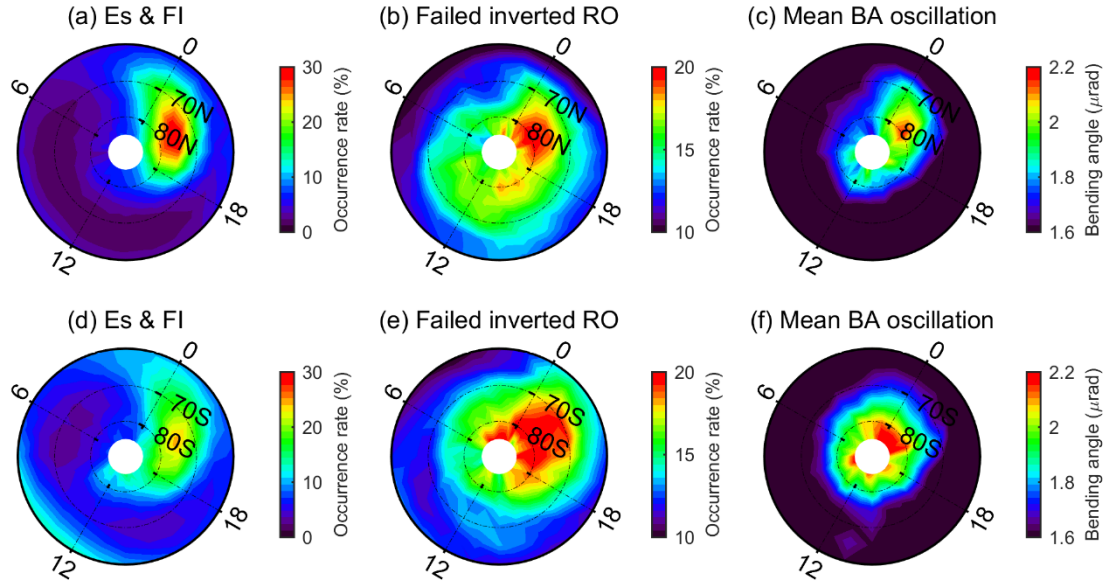
Figure 4. MLT-MLat variation of the Es and F layer irregularity occurrence rate (left panels), the failed inverted RO occurrence rate (middle panels), and the mean bending angle oscillation (right panels) in polar regions. Please note that the top panels represent the results in northern polar regions while the bottom panels denote the southern polar regions.

485
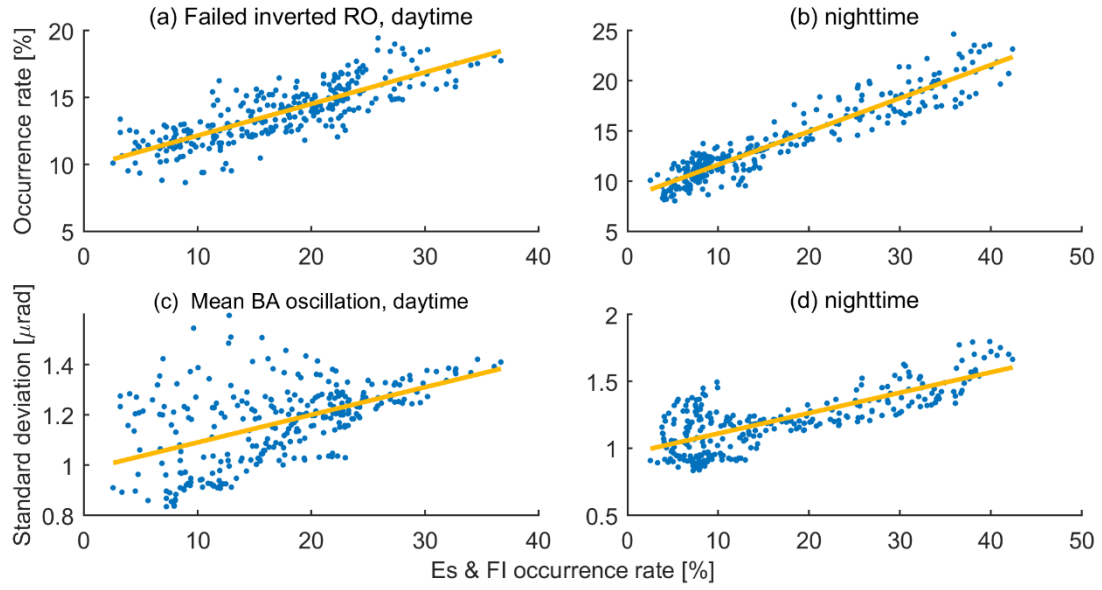
486   **Figure 5. Correlations between the ionospheric irregularity and the two parameters in middle and**

487   **low latitudes (60° S-60° N) during the daytime (6~18 MLT, left panels) and nighttime (0~6 & 18~24**

488   **MLT, right panels) of 2011-2013. The yellow line is the corresponding linear least square fitting**

489   **results.**

490
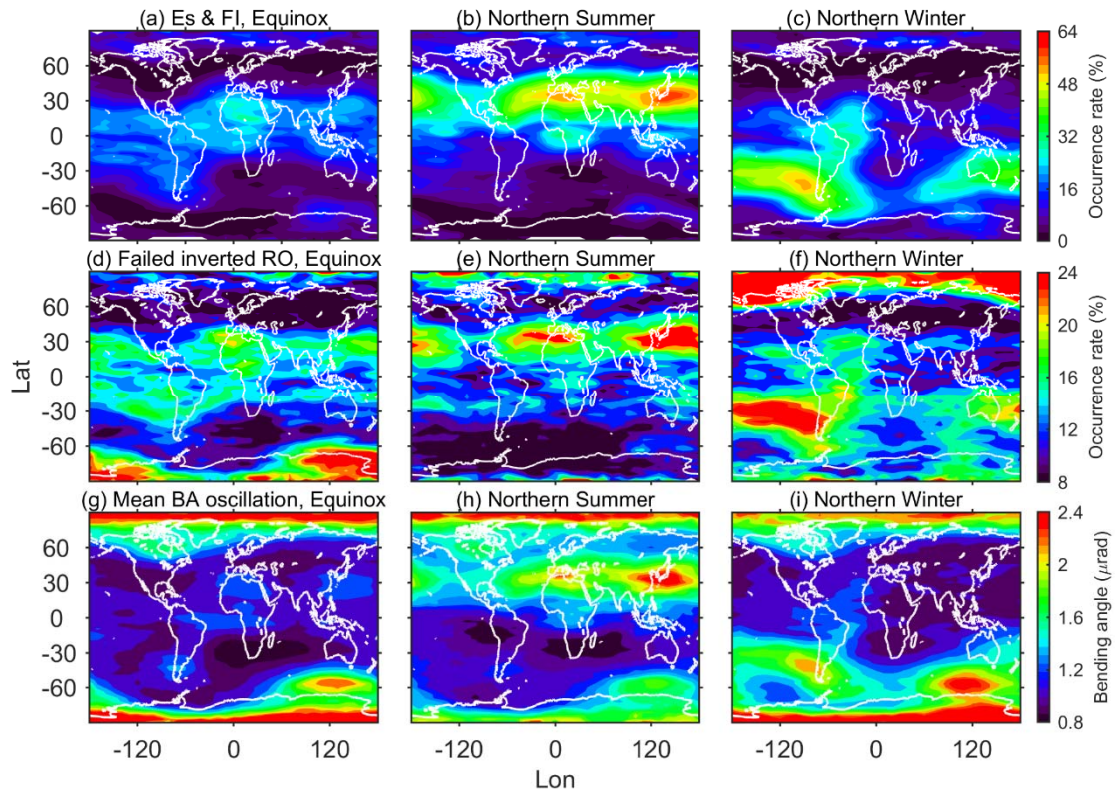
491 **Figure 6. Global geographical distribution of the Es and F layer irregularity occurrence rate (top**

492 **panels), the failed inverted RO occurrence rate (middle panels), and the mean bending angle**

493 **oscillation (bottom panels) for Equinox (left panels), Northern Summer (middle panels), and**

494 **Northern Winter (right panels).**

495
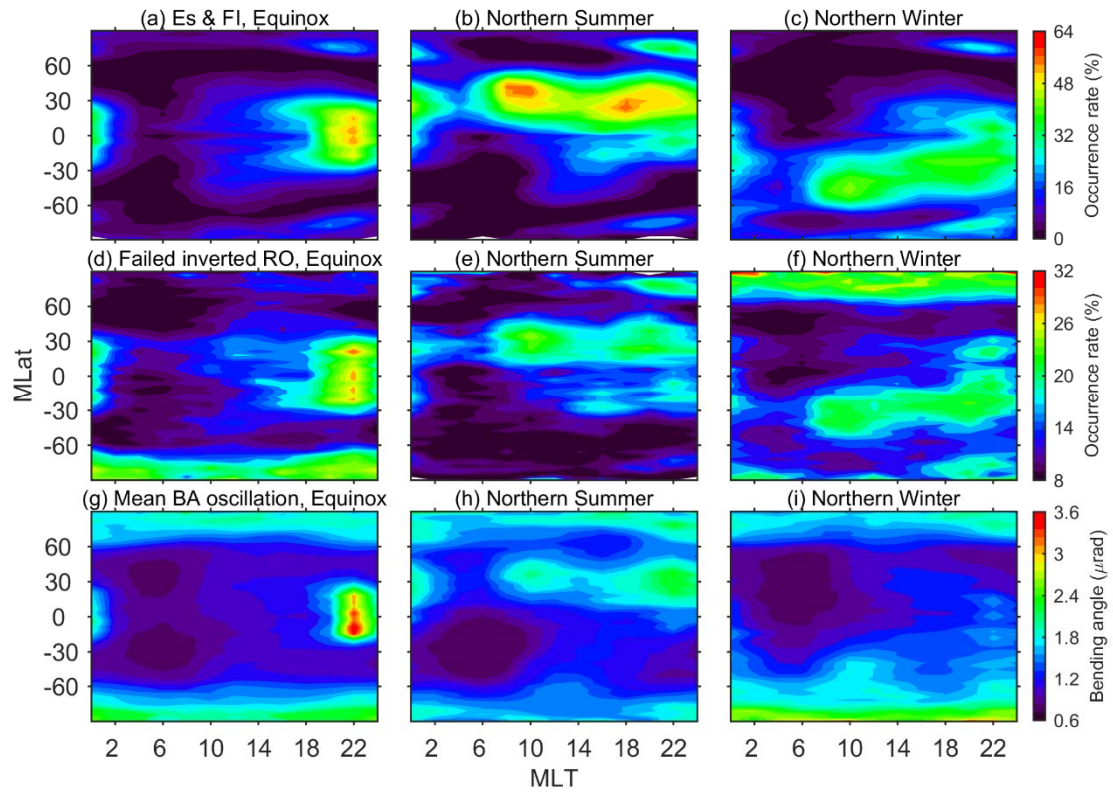
Figure 7 The same as Figure 6, but for geomagnetic local time (MLT) and geomagnetic latitude

(MLat) variation.